Journal of Materials Chemistry A

Li^+ Storage and Transport in High-Voltage Spinel-Type $LiNi_{0.5}Mn_{1.5}O_4$ Codoped with F^- and Cu^{2+}

Journal:	*Journal of Materials Chemistry A*
Manuscript ID	TA-ART-10-2022-008199.R2
Article Type:	Paper
Date Submitted by the Author:	01-Dec-2022
Complete List of Authors:	Kim, Dae-wook; KITECH, Ulsan Regional Division Shiiba, Hiromasa; Shinshu University, Department of Materials Chemistry Teshima, Katsuya; Shinshu University, Department of Materials Chemistry; Shinshu University, Center for Energy and Environmental Science Zettsu, Nobuyuki; Shinshu University Graduate School of Engineering Faculty of Engineering, Materials Chemistry

ARTICLE

Li^+ Storage and Transport in High-Voltage Spinel-Type $LiNi_{0.5}Mn_{1.5}O_4$ Codoped with F^- and Cu^{2+}

Received 00th January 20xx,
Accepted 00th January 20xx

DOI: 10.1039/x0xx00000x

Dae-wook Kim,[a, ‡] Hiromasa Shiiba,[a, ‡] Katsuya Teshima,[a, b] and Nobuyuki Zettsu, [a, b, c]

The electrochemical, structural, and Li^+ transport properties of dual Cu^{2+}/F^--doped $LiNi_{0.5}Mn_{1.5}O_4$ ($LiNi_{0.5}Mn_{1.49}Cu_{0.01}O_{4-x}F_x$) cathodes were probed both experimentally and theoretically and were found to strongly depend on F^- content (i.e., *x*). Notably, some features of single Cu^{2+}- and F^--doped materials were simultaneously observed within a certain narrow range of *x*. $LiNi_{0.5}Mn_{1.49}Cu_{0.01}O_{3.94}F_{0.06}$ (ordered $P4_332$ space group) showed the best reversible specific capacity, C-rate capability, and cyclability within the operating voltage range of 3.5–4.8 V vs. Li^+/Li, while the highly fluorinated $LiNi_{0.5}Mn_{1.49}Cu_{0.01}O_{3.94}F_{0.12}$ (disordered *Fd*-3*m* space group) delivered a reversible discharge capacity of >200 mAh g^{-1} at cut-off voltages of 4.8–2.0 V without any significant capacity fading over 50 cycles. The results of density functional theory–based simulations and experimental measurements suggested that dual doping significantly changed the electronic structure, reduced the activation energy of Li^+ hopping to neighboring octahedral vacancies, and alleviated lattice distortion caused by the insertion of extra Li^+ into the spinel framework, thus suppressing the irreversible transition from the spinel phase to tetragonal phases.

Introduction

Despite their widespread use in transportation systems such as electric and plug-in hybrid vehicles, Li-ion batteries (LIBs) suffer from certain unresolved scientific and technical problems such as insufficient energy density and C-rate capability, high cost, and poor elemental stability (especially in the case of Co-containing materials).[1,2] Most of these problems can be mitigated by addressing the inherent disadvantages of LIB cathodes, e.g., their low specific capacity, leaching of transition metal ions into electrolytes at high voltages, impedance growth due to the formation of thick cathode electrolyte interface (CEI) layers, O_2 gas evolution, and overly high Co content.

Since the first use of $LiCoO_2$ as a cathode material in prototype LIBs, numerous materials capable of reversible electrochemical Li^+ insertion have been developed and commercialized, as exemplified by layered Ni-rich $LiNi_{0.82}Co_{0.15}Al_{0.03}O_2$, $LiNi_{0.3}Co_{0.3}Mn_{0.3}O_2$, spinel-type $LiMn_2O_4$, olivine-type $LiFePO_4$, and disordered rock-salt-type Li-rich compounds.[3-9] The energy density of a battery is determined by its working voltage, specific capacity, and electrode density. $LiNi_{0.5}Mn_{1.5}O_4$ (LNMO), which has recently attracted much attention as a cathode material for next-generation energy storage systems, provides the advantages of a high operating voltage (4.8 V vs. Li/Li^+) and the absence of Co. Research on Li-rich spinel-type $Li_{1+y}Ni_{0.5}Mn_{1.5}O_4$ suggests that the reduction of all Mn ions to Mn(III) should afford $Li_{2.5}Ni_{0.5}Mn_{1.5}O_4$ and achieve a theoretical specific capacity of 347 mAh g^{-1}.[10-13]

However, the commercialization of spinel-type LNMO is hindered by the side reactions occurring at the electrode/electrolyte interface during high-voltage operation and the irreversible cubic-to-tetragonal phase transition upon extra Li^+ insertion. Moreover, the operating potential range of LNMO extends beyond the electrochemical stability window of standard organic carbonate-based electrolytes, which can lead to excessive electrolyte decomposition, reduced battery lifetime, and possible safety risks. The partially delithiated LNMO surface is strongly Lewis-basic, thus promoting side reactions associated with the oxidative decomposition of the electrolyte and inducing significant capacity degradation upon cycling.[14-16] Although the theoretical specific capacity of Li-rich spinel-type LNMO is far beyond that reported to date for high-Ni layered oxides and Li-Mn-rich materials, LNMO suffers from rapid capacity fading upon extra Li^+ insertion because of the occurrence of the abovementioned cubic-to-tetragonal phase transition.[12] Despite the fact that the corresponding reaction mechanism has been well studied, several problems related to inner space control in the LNMO framework for the reversible storage of extra Li^+ ions and their diffusion characteristics remain unsolved.[17-19]

Manthiram *et al.* revealed the importance of Mn^{3+} content control for tuning the electrochemical characteristics of spinel-type LNMO.[20-24] The substitution of Ni^{2+} and/or Mn^{4+} by transition metal (e.g., Cr, Fe, Mg, Zn, or Ru) cations is a plausible way of tuning the valence state of Mn, which largely determines

[a] *Department of Materials Chemistry, Faculty of Engineering, Shinshu University, 4-17-1 Wakasato, Nagano 380-8553, Japan*
[b] *Research Initiative for Supra-Materials, Shinshu University, 4-17-1 Wakasato, Nagano 380-8553, Japan*
[c] *Energy Landscape Architectonics Brain Bank (ELab²), Shinshu University, 4-17-1 Wakasato, Nagano 380-8553, Japan*
‡ *These authors contributed equally*

Electronic Supplementary Information (ESI) available: Additional characterization details of the examined electrode materials (structure, Li^+ migration pathway and kinetics, and composition). See DOI: 10.1039/x0xx00000x

the ordering of $Li^+/Ni^{2+}/Mn^{4+}(Mn^{3+})$ arrangements in the spinel structure in conjunction with oxygen deficiency formation. Moreover, this substitution allows one to change the degree of Ni/Mn ordering, morphology, and Mn^{3+} content and thus enhance electrochemical performance. The above authors identified the Ni^{2+}/Mn^{4+} arrangement determining half-cell performance when the cell is operated within a limited working voltage range of 3.5–4.8 V vs. Li/Li^+ and demonstrated that the trace-level substitution of Ni^{2+} for Fe^{3+} (e.g., in $LiNi_{0.42}Fe_{0.08}Mn_{1.5}O_4$) in LNMO afforded one the best-performing materials.[23] The introduction of a small number of Cu^{2+} at Mn^{4+} site was shown to promote the Ni^{2+}/Mn^{4+} ordering arrangement associated with the *Fd*-3*m* → *P*4$_3$32 transition in oxygen-deficient $LNMO_{4-\delta}$. Although this transition occurred in the local space near the defect annihilation point, it affected macroscopic electrochemical properties.[25]

Recently, we have demonstrated that the stabilization of LNMO surfaces by direct ionization potential tuning (LUMO-level engineering) through the formation of mixed-anion surfaces is a promising means of increasing high-voltage durability. The partial substitution of oxygen vacancies with F^- or S^{2-} significantly impacted electrochemical properties and resulted in a crystal field splitting more complex than that produced by cation substitution.[26,27] Moreover, Li^+ diffusion behavior, morphology, and Fermi level shifts depended on the type of the introduced anion. Although the respective mechanisms were different, the mixed-anion surface provided a thinner CEI layer than stoichiometric LNMO and oxygen-deficient $LNMO_{4-\delta}$ surfaces. Furthermore, anion substitution affected the activation barrier of Li^+ hopping along the most energetically preferable 8a-16c-8a pathway by influencing the size of the bottleneck and interactions with Li^+.

The results of previous studies suggest that simultaneous trace-level substitutions of Cu^{2+} for the stabilization of *P*4$_3$32 phase in $LNMO_{4-\delta}$ and F^- for the enhancement of both Li^+ diffusion behavior and the mitigation of side reaction with electrolyte can produce significant changes in structural and electrochemical characteristics. The motivation for selecting Cu^{2+} is based on our computational studies on the extrinsic defect formation energies via elemental substitution of Mn site with four period of transition metal species. It revealed that only Cu^{2+}stabilized stabilizing *P*4$_3$32 symmetry (ordered Ni/Mn arrangement) in oxygen-deficient $LNMO_{4-\delta}$. Zn^{2+} was also one of the other candidates for the stabilization of Ni/Mn arrangements ordering in $LNMO_{4-\delta}$, however the incorporated Zn^{2+} promote to generate anti-site defects with Li^+, leading to significant capacity degradation. Since varying each sublattice space implies significant changes in the electronic structure, it is suggested that changes in the more complex coordination environment caused by simultaneous doping of both cations and anions allow the electrochemical properties of LNMO-based cathode materials to be tuned over a wide range. Herein, we perform both experimental and theoretical studies to investigate the Li^+ storage and transportation properties of F^-/Cu^{2+}-codoped spinel-type $LiNi_{0.5}Mn_{1.5}O_4$ to attain the desired electrochemical performance during charge-discharge, considering that the overall reaction involves Ni^{2+}/Ni^{4+} (4.7 V), Mn^{3+}/Mn^{4+} (4 V), and Mn^{4+}/Mn^{3+} (<3 V) redox couples.

Results and discussion

Structural characterization

Crystalline $LiNi_{0.5}Mn_{1.49}Cu_{0.01}O_{4-x}F_x$ ($LNMCOF_x$, x = 0.03, 0.06, 0.12) was synthesized in two steps. Specifically, crystalline $LiNi_{0.5}Mn_{1.49}Cu_{0.01}O_4$ (LNMCO) was prepared in molten LiCl-KCl and then heated with LiF-KCl at 800 °C for 20 h.[25,28] The content of F^- was controlled by the LiF feed ratio. The contents of Li, Ni, Cu, and Mn were evaluated using Inductively coupled plasma-optical emission spectroscopy (ICP-OES), while those of O and F were evaluated using core-level X-ray photoelectron spectroscopy (XPS). The compositions of the prepared materials are listed in Table S1. For instance, the atomic percent of F and O in the $LNMCOF_{0.12}$ crystal were 0.60 at% of F and 20.02 at% of O, respectively. The atomic percentage can be converted to F/O ratio of O - 97.09 mol%, F - 2.91 mol% and converted to a composition of $O_{3.88}$ $F_{0.12}$.

Figures 1(a–c) show the F 1*s* spectra of $LNMCOF_x$ recorded for different depths from the surface, revealing that in all cases, the F 1*s* signal became extremely weak at a depth of 20 nm and disappeared at a depth of 40 nm. This behavior indicated that F content decreased with increasing depth, suggesting that F^- ions concentrated at the crystal surface. A similar trend was observed for $LiNi_{0.5}Mn_{1.5}O_{4-x}F_x$ ($LNMOF_x$) crystals.[26] F^- preferentially passivated the oxygen vacancy formed at the surface to stabilize the crystal surface, leading to make surface energy lower. According to the results of powder X-ray diffraction (XRD) analysis (Figure 1(d)), all samples contained disordered LNMO with *Fd*-3*m* symmetry irrespective of F content. Notably, the lattice parameter of $LNMCOF_x$ (extracted from the corresponding XRD patterns) slightly increased upon the introduction of F^- (Figure 1(e)), possibly because of the formation of Jahn-Teller-distorted Mn^{3+} ions associated with charge compensation due to the introduction of F^- and lattice expansion due to electrostatic repulsion between neighboring anions caused by the introduction of the high-charge-density F^- anions. The local Ni^{2+}/Mn^{4+} arrangements were probed by Raman spectroscopy (Figure 1(f)).[29,30] The strong bands at 635 and 494 cm^{-1} were assigned to the symmetric stretching (A_{1g}) of Mn–O bonds in octahedral MnO_6 units and the stretching of Ni^{2+}–O bonds, respectively. The peak at 580–606 cm^{-1} corresponded to the T_{2g} stretching mode of spinel-type compounds, and the splitting of this peak reflected the presence of an ordered structure in the spinel framework. The broadening of Raman signals with increasing F^- content suggested that the local *P*4$_3$32 symmetry was transformed to *Fd*-3*m* in $LNMCOF_{0.12}$ crystals. Thus, the stabilization of the local Ni^{2+}/Mn^{4+} orientation driven by Cu^{2+} introduction was maintained up to $LNMCOF_{0.06}$. The antagonistic effects of Cu^{2+} and F^- doping on the local Ni^{2+}/Mn^{4+} orientation were highly balanced, which indicates that features due to single Cu^{2+} and/or F^- doping could be simultaneously observed within a

very narrow range of *x*. The proportion of Mn^{3+}/Mn^{4+} examined by XPS Two peaks attributed to Mn^{3+} and Mn^{4+} were observed in the Mn 2p core-level spectra (Figure 1(g)). The Mn^{3+}/Mn^{4+} ratio was 0.55 for the ordered LNMO and increased with F^- substitution, which agrees with our computational predictions (0.63 for $LNMCOF_{0.03}$, 0.77 for $LNMCOF_{0.06}$ and 1.67 for $LNMCOF_{0.3}$). XPS Mn2p spectroscopic futures suggest that the F^- incorporation into LNMCO lattice highly randomizes the local Ni/Mn arrangement.

Field-emission scanning electron microscopy imaging (Figures 1(h–k)) showed that stoichiometric LNMO formed octahedral crystals with distinct facets and an average diameter of ~1.0 μm. The analysis of particle size by laser diffraction revealed that the introduction of a small amount of Cu_{Mn} (LNMCO) decreased the average crystal size from 1.0 to 0.7 μm.[25] Furthermore, the introduction of F^- ($LNMOF_x$) induced the change from the octahedral shape to a truncated polyhedral shape. Cu^{2+}/F^- codoping resulted in morphological changes including particle size reduction and truncation at particle edges and tops. Notably, the axial length of the octahedron was anisotropically extended by F^- incorporation, as reflected by the Jahn-Teller distortion generated in uniaxially oriented $MnO_{6-x}F_x$ octahedra. In addition, step-terrace structures with regular periodicity were formed on the {111} planes of the crystal surface, possibly indicating a change in surface energy.

Electrochemical characterization (4.8-3.5 V)

Lithium-ion storage properties

Figure 2(a) presents typical half-cell charge-discharge curves recorded at a rate of 0.2 C, showing that a distinct voltage plateau starting from 4.6–4.8 V vs. Li/Li^+ was observed for stoichiometric LNMO and LNMCO. This behavior suggested that electrochemical delithiation/lithiation was mainly promoted by the two-phase reaction associated with Ni^{2+}/Ni^{3+} and Ni^{3+}/Ni^{4+} redox couples. Thus, the Mn^{3+}/Mn^{4+} redox couple barely contributed to electrochemical intercalation. The above charge-discharge behavior was characteristic of the ordered LNMO phase. In contrast, an inflection point at ~4.0 V due to the contribution of the Mn^{3+}/Mn^{4+} couple was observed for the highly fluorinated $LNMCOF_{0.12}$/Li half-cell, which supported the formation of a disordered cation (Li/Ni/Mn) arrangement in $LNMCOF_{0.12}$ and agreed with the results of Raman spectroscopic analysis. The evaluation on the contribution of Mn^{3+}/Mn^{4+} redox pair to specific capacity on the discharge curves were summarized in Table S2. It indicates that the F^- incorporation found to increase the contribution by the Mn^{3+}/Mn^{4+} redox pair. Thus, the results of structural and electrochemical analysis demonstrated that the presence of external defects in LNMCO stabilized the local ordering of Li/Ni/Mn cations, whereas fluorination induced the degradation of the ordered cation arrangement. The local cation-ordered array structures observed near Cu_{Mn} defects completely disappeared in $LNMCOF_{0.12}$.

The electrochemical reaction mechanism of $LNMCOF_x$ was further studied using cyclic voltammetry (CV). As shown in Figure 2(b), the broadened oxidation peak at ~4.7 V observed for LNMCO was split into two sharp peaks in the case of $LNMCOF_x$. Furthermore, the polarization extent decreased with increasing F^- content. This behavior was ascribed to the occurrence of solid-solution reactions involving Ni^{2+}/Ni^{3+} and Ni^{3+}/Ni^{4+} redox pairs and was related to the formation of steps in the low-Li-content region of the voltage profile.[31,32] Thus, F^- incorporation stabilized the intermediate composition in delithiated $L_{1-y}NMCOF_x$ and led to the narrowing of $Ni^{2+}/Ni^{3+}/Ni^{4+}$ electrochemical potential gaps. The expansion of the solid-solution reaction range upon the introduction of F^- was more likely to promote Li^+ diffusion in the bulk than the two-phase reaction, as no significant lattice differences were present at the phase boundary.[33] Note that the LNMCO cathode exhibited a higher current density than the $LNMCOF_x$ cathode at high voltages ranging from 4.8 to 5.0 V. The origin of the current is assigned to the decomposition of the organic electrolyte at the electrode interface; thus, this result shows that the F incorporation prevented the side reaction with the electrolyte, leading to mitigate their impedance growth as well as their capacity fading during cycling.

Subsequently, we performed density functional theory (DFT) calculations to probe the correlation between the electrochemical properties and fine structure of $LNMCOF_x$ as well as to evaluate total energies for various Li contents. Figure S2 shows the DFT-calculated atomic arrangements of the most stable $LiNi_{0.5}Mn_{1.49}Cu_{0.01}O_{4-x}F_x$ ($LiNi_{0.5}Mn_{1.375}Cu_{0.125}O_{4-x}F_x$ in 56-atom supercell) structures for (a) x = 0.125 (single F^- incorporation into the supercell, $Li_8Ni_4Mn_{11}Cu_1O_{31}F_1$), (b) x = 0.250 (double F^- incorporation, $Li_8Ni_4Mn_{11}Cu_1O_{30}F_2$), and (c) x = 0.375 (triple F^- incorporation, $Li_8Ni_4Mn_{11}Cu_1O_{29}F_3$). Details of the most stable structures of each compound analyzed by DFT calculations, including the Ni^{2+}/Mn^{4+} antisite defect formation energies and the changes in lattice constants (shown in Figure 1(e)), are explained in the supplementary material. Figures 2(c–e) show formation energy as a function of Li content in DFT-modeled $LNMCOF_x$ frameworks (x = 0.125, 0.25, 0.375). For $LNMCOF_{0.125}$, only the $Li_{0.125}$ composition stably formed a delithiated phase with a Li composition intermediate between $Li_{1.0}$ and Li_0 compositions. In contrast, the total energies of delithiated phases with various Li contents decreased with increasing F^- content. $Li_{0.875}$, $Li_{0.750}$, $Li_{0.625}$, and $Li_{0.125}$ phases were stably formed in $LNMCOF_{0.375}$. The stabilization of the intermediate composition in $L_{1-y}NMCO$ via F^- doping contributed to the shift of the dominant reaction mechanism from the two-phase reaction to a solid-solution reaction in which the amount of Li stored in the spinel framework continuously changes during charging. This conclusion was consistent with the CV results shown in Figure 2(b).

The specific capacity of $LNMCOF_x$ strongly depended on F^- content. The half-cell with the $LNMCOF_{0.06}$ electrode (intermediate extent of F^- incorporation) showed a maximum specific capacity of 128 mAh g^{-1}. The corresponding value of $LNMCOF_{0.03}$ was 4–5% lower, even though both systems exhibited Ni^{2+}/Mn^{4+} ordered phases, according to the results of

Raman spectroscopy analysis. DFT calculations (Figures 2(c–e)) indicated that the difference between the total energy of the most stable structures of $Li_{0.125}$ and Li_0 compositions was larger for $LNMCOF_{0.125}$ than for $LNMCOF_{0.250}$. Further delithiation above $Li_{0.125}$ was inhibited in $LNMCOF_x$ with a very small F^- content. Specific capacity reduction was not observed for $LNMCOF_x$ with moderate F^- content. Furthermore, a large formation energy gap was observed for $LNMCOF_{0.375}$ ($Li_8Ni_4Mn_{11}Cu_1O_{29}F_3$) in the low-Li-content region ($L_{0.125}NMCOF_{0.375}$). This behavior was similar to that observed for x = 0.125 and was consistent with the experimentally observed capacity reduction in the $LNMCOF_{0.12}$/Li half-cell (excessive F doping).

We further analyzed the redox-active centers in a series of $LNMCOF_x$ systems. Figures 2(f–h) show the DFT-calculated partial density of states (PDOS) for the Mn 3*d* and Cu 3*d* orbitals in $LNMCOF_x$ materials with various Li contents, while Table S3 summarizes changes in the average oxidation state in response to delithiation. For x = 0.125 and 0.25(single and double F^- incorporation per unit cell), no PDOS changes were observed for Mn 3*d* orbitals in the full range of Li content ($Li_{1.0}$ to Li_0), which indicated that the oxidation state of Mn was preserved as Mn^{4+} with a t_{2g}^3 electron configuration. Only in the case of x = 0.25, the presence of two Cu 3*d* orbitals in the conduction band indicated a $t_{2g}^6e_g^2$ electron configuration. The Cu 3*d* PDOS profile drastically changed in the first voltage step of the charging reaction, which corresponded to the transition from $Li_{1.0}$ to $Li_{0.875}$. As no changes were observed in the further delithiation process, we concluded that Cu^{2+} was fully oxidized to be exclusively present as Cu^{3+} until the $Li_{0.875}$ composition was reached in $LNMCOF_{0.25}$. In contrast, the Ni 3*d* PDOS profile continuously changed in the voltage step of the charging reaction, which corresponded to the transition from $Li_{0.875}$ to Li_0. Thus, the oxidation reaction center was identified as $Ni^{2+}/Ni^{3+}/Ni^{4+}$, and all Li^+ ions could be electrochemically extracted during charging (Figure S2(a), (b)).

For x = 0.375 (triple F^- incorporation per unit cell), the Mn 3*d* band appeared near the Fermi level, indicating the presence of a mixed +3/+4 oxidation state. In addition, the valence state of Cu in the $Li_{1.0}$ composition was determined as +2. As delithiation progressed from $Li_{1.0}$ to $Li_{0.125}$, all PDOS profiles moved closer to the Fermi level, which implies that the deintercalation of Li^+ was associated with charge compensation through the electrochemical oxidation of Cu^{2+} to Cu^{3+}, Mn^{3+} to Mn^{4+}, and Ni^{2+} to Ni^{4+}.(Figure 2(h) and S2(c)) The low specific capacity experimentally observed for highly fluorinated $LNMCOF_{0.12}$ (Figure 2(a)) was closely related to the stabilization of Mn^{3+} via $–F^–Mn^{3+}–F^–$ bonding. This bonding was associated with the stabilization of the d_{z^2} orbital and increased the formation energy of the highly delithiated phase as well as the oxidation potential of Mn^{3+}.

C rata capability (4.8-3.5 V)

The C-rate capabilities of $LNMCOF_x$ half-cells were determined by systematic galvanostatic charge-discharge testing at various current densities (Figure 3(a, b)). Previous works showed that the introduction of extinct Cu_{Mn} defects into the spinel framework improves C-rate capability by increasing electrical conductivity via *d*-electron doping and reducing the activation energy of Li^+ hopping along the most energetically preferable 8c-4a/12d-8c route.[25] The overpotential of the LNMO electrode observed as higher discharging rate is reduced by Cu^{2+} substitution and further F^- substitutions The specific capacities of $LNMCOF_{0.06}$ and $LNMCOF_{0.12}$ half-cells at 10 C were determined as 100 and 110 mAh g^{-1}, respectively. The higher (compared to those of LNMO and LNMCO) capacity retentions observed for $LNMCOF_x$ electrodes, which were prepared with a relatively high active material loading (>10 mg cm^{-2}) and density (>3.0 g cm^{-3}), were ascribed to the synergetic effects of Cu^{2+} and F^- codoping on electrical and ionic conductivities. The kinetic parameters of Li^+ migration, that is, the electrode resistance and Li^+ diffusion coefficient (D_{Li}), were evaluated using electrochemical impedance spectroscopy. The representative Nyquist plots of the examined half-cells (Figure 3(c)) featured semicircles containing multiple (high- and low-frequency) relaxation components with different time constants, and the shapes of these semicircles were strongly dependent on doping extent and type. Impedance parameters were analyzed using Bode diagrams and an equivalent circuit model. The high-frequency component represented the resistance of the surface film (R_{sf}: CEI layer), while the low-frequency component represented charge-transfer resistance (R_{ct}). Both R_{sf} and R_{ct} were smaller for the LNMCO/Li half-cell than for the $LNMO_{4-d}$ electrode system, which well agreed with the C-rate capability trend. In contrast, significant reductions in both R_{sf} and R_{ct} were observed for the $LNMCOF_{0.06}$ electrode system, with further F^- doping leading to progressive kinetic parameter degradation (Table S4). The trajectory of Li^+ migration along the most energetically preparable 8c–4a/12d–8c pathway in the spinel framework and the activation energy for the corresponding Li^+ hopping were studied using DFT calculations (Figure 3(d)). The results indicated that the Li^+ ions in the spinel framework have the lowest activation energy and therefore preferentially travel along the 8c-4a/12d-8c route regardless of the degree of F^- doping. The most energetically favorable Li^+ migration pathway in each $LNMCOF_x$ system did not involve F^- ions in octahedral vacancy sites, which was attributed to the increase in the activation barrier for Li^+ hopping along the 8a-16c-8a pathway due to electrostatic repulsion between V'_{Li} at 8c-4a/12d-8c sites and $O_O^\times$, $V_O^{\cdot\cdot}$, or $F_O^{\cdot}$ at 24e sites, as observed for LNMOF systems.[26] In stoichiometric LNMO, the Li^+ ions followed a linear trajectory, whereas in LNMOF, they tended to move in a meandering fashion. Interestingly, the coordination of Cu ions to oxygen occupying the 24e sites of the octahedral Li^+ vacancies in the Li^+ migration pathway decreased the activation energy of Li^+ hopping. As the CuO_5F_1 octahedron containing Cu^{2+} ions with a d^9 configuration was highly distorted because of the Jahn-Teller effect, the coexistence of Cu^{2+} and F^- may have reduced the effect of the electrostatic repulsion–caused increase in the activation barrier by modulating the size of the Li^+ diffusion bottleneck.

Cyclability (4.8-3.5 V)

Galvanostatic charge-discharge tests were performed at a cutoff voltage of 4.8–3.5 V to examine the effect of Cu^{2+} and F^- doping on cyclability. The cyclabilities of all $LNMCOF_x$ systems exceeded that of stoichiometric LNMO (Figure 4(a)). In particular, $LNMCOF_{0.12}$ showed the highest capacity retention after 200 cycles, and its Coulombic efficiency remained above 99%. In contrast, significant capacity degradation was observed for the LNMO electrode. The results of impedance spectroscopy measurements taken from the cycled cell showed that all kinetic parameters (R_{sf}, R_{ct}, and D_{Li}) degraded after cycling, which was mainly ascribed to the leaching of transition metal cations associated with the oxidative decomposition of the electrolyte at the electrode surface.[28] Note that this degradation was significantly mitigated by the incorporation of F^- into LNMCO, with the $LNMCOF_{0.12}$/Li cell showing the most significant impedance growth (Figure 4(b) and Table S4).

The effect of F^- introduction on the electronic structure of the LNMCO surface was further investigated using valence band spectroscopy. As shown in Figure 4(c), the position of the valence band edge shifted to deeper levels with increasing extent of F^- doping. Furthermore, the Mn 3*d*, O 2*p*, and O 2*s* spectra revealed an overall shift of the related valence band peaks to lower energies. These spectral changes suggested that highly electronegative F^- doping reduced the electron-donating nature of the electrode surface via the enhanced ionic bonding characteristics and thus helped to suppress the oxidative decomposition of the electrolyte. This electrode surface stabilization due to F^- doping was concluded to be an effective approach for hindering impedance growth associated with the overgrowth of the highly resistive CEI layer upon charge-discharge cycling.

Electrochemical characterization (4.8-2.0 V)

Finally, the synergistic effects of Cu^{2+}/F^- codoping on the reversible specific capacity of Li-rich spinel-type $Li_{1+y}Ni_{0.5}Mn_{1.5}O_4$ due to excess Li^+ insertion in association with the abovementioned phase transition were studied by galvanostatic discharge tests at a cutoff voltage extended to 2.1 V. The structural distortion inside the LNMO lattice due to the excess insertion of Li^+ (Li > 1) allowed us to more clearly visualize the codoping-induced Li^+ diffusion pathway and spatial structure changes inside the LNMO lattice. Figure 5(a) shows typical discharge profiles based on the extra lithiation reaction, revealing that two-step voltage plateaus were observed irrespective of cation ordering or F^- content. This finding indicates that lithiation was accompanied by a two-phase reaction. In addition, the voltage step can be explained by assuming phase transitions from cubic to tetragonal structures. The specific capacity of $LNMCOF_x$ strongly depended on F^- content (which, in turn, influenced cation ordering) and was largest (254 mAh g^{-1} at 2.75 V and 284 mAh g^{-1} at 2.1 V) for $LNMCOF_{0.06}$ ($P4_332$ symmetry). In this case, ~1.9 Li^+ ions per formula unit were electrochemically inserted into the spinel framework. Dual doping significantly increased the Li^+ storage capacity of stoichiometric LNMO, which has so far been the highest among all reported materials. In contrast, hardly any changes in specific capacity were observed for $LNMO_{4-\delta}$ and $LNMCOF_{0.12}$ with *Fd*-3*m* symmetry, which exhibited the same voltage slopes in their discharge profiles and specific capacities of ~55 mAh g^{-1} in the voltage range of 2.5–2.0 V. These results indicated that capacity enhancement was only noticeable within a very narrow range of conditions corresponding to the orderly arrangement of metal cations in the spinel lattice.

We further studied structural changes during Li^+ insertion/deinsertion in Li-rich $LNMCOF_x$. Figures 5(b, c) show the *ex situ* XRD profiles of $LNMCOF_{0.12}$ and $LNMCOF_{0.06}$ electrodes with various states of charge, with the peaks of the tetragonal phase (*I*41/*amd* space group) displayed as a reference (dashed lines). The electrodes subjected to voltages of 2.7 or 2.5 V contained both cubic and tetragonal phases. In sharp contrast to the case of $LNMCOF_{0.12}$, the splitting of the tetragonal phase peaks at $2\theta = 18°$ was observed at 2.7 V for $LNMCOF_{0.06}$. With increasing Li content (2.5 V), the peaks of the cubic phase lost intensity, whereas those of the tetragonal phase gained intensity. These results indicated that the cubic-to-tetragonal phase transition proceeded more significantly in $LNMCOF_{0.06}$ than in $LNMCOF_{0.12}$. The percentage of the tetragonal phase in $P4_332$-type $LNMCOF_{0.06}$ exceeded that in *Fd*-3*m*-type $LNMCOF_{0.12}$, and the numbers of Li^+ ions inserted per formula unit at 2.7 V were determined as 1.5 and 1.2, respectively. At 2.5 V, a clear peak splitting associated with the above phase transition was observed, at which point the number of Li^+ ions inserted per formula unit increased to 1.6 for $LNMCOF_{0.06}$ and 1.4 for $LNMCOF_{0.12}$.

Figure 5(d) shows the effects of applied potential (4.8–2.0 V) on the lattice constant and lattice volume of LNMO and $LNMCOF_x$ determined from *ex situ* XRD profiles. The lattice constant of LNMO in the fully delithiated state (i.e., that present at 4.8 V) gradually increased upon Li^+ insertion. Distinctive doping extent–dependent changes in lattice parameters were observed below 2.7 V. The simultaneous observations of both cubic and tetragonal phase peaks in XRD profiles indicated that lithiation proceeded through the two-phase reaction. The lattice constant of the cubic phase remained unchanged after the cubic-to-tetragonal phase transformation in all cases, and that of the tetragonal phase increased with increasing Li content, which suggested that extra Li^+ was electrochemically inserted into the octahedral Li vacancies of the spinel framework.

The two voltage plateaus observed for the extra Li^+ insertion below 3 V (2.75 and 2.1 V) were further examined using DFT calculations. Figure S3 shows the most stable atomic configurations of $L_{1.125}NMCOF_x$ ($P4_332$ symmetry group) with various amounts of F^- per unit cell, suggesting that extra Li^+ ions occupy empty octahedral sites in the spinel lattice. The Li^+ ions inserted into these sites are believed to promote the diffusion of nearest-neighbor Li^+ ions occupying tetrahedral sites to adjacent octahedral sites with relatively large volumes under the action of ionic repulsion (Figure S4). Further electrochemically inserted excess Li^+ ions preferentially occupy

the 12d sites, which gives rise to other plateaus in the discharge profile. On the other hand, in the case of *Fd*-3*m* spinel, Li^+ vacancies are restricted to crystallographically equivalent 16c sites. As the volume of the 4a site is larger than that of the 16c site, the former sites of $P4_332$ spinel are more energetically suitable for the insertion of excess Li^+. Figure S5 presents the calculated volume, quadratic elongation, and bond angle variances for octahedral Li^+ vacancy sites in the Li^+ diffusion path of bare LNMCO and $LNMCOF_x$, demonstrating that the Li^+ vacancy site space volume was larger in $LNMCOF_x$ than in LNMCO. Thus, F^- doping contributed to site volume expansion to facilitate the storage of excess Li^+.

The cycling stabilities of LNMO and $LNMCOF_x$ were studied to determine the impact of codoping on the mitigation of irreversible capacity loss. As shown in Figure 5(e), cyclability was strongly dependent on the local cation arrangement in $LNMCOF_x$. For instance, the first charge capacity of ~250 mAh g^{-1} observed for $P4_332$-type $LNMCOF_{0.06}$ decreased to 185 mAh g^{-1} (capacity retention = 75%) after 50 cycles. The *Fd*-3*m* type $LNMCOF_{0.12}$/Li cell delivered the highest capacity retention of 92% despite exhibiting a first discharge capacity (200 mAh g^{-1}) smaller than that of $P4_332$-type $L_{1.6}NMCOF_{0.06}$. Although the effect of capacity degradation associated with the oxidative decomposition of the electrolyte in the high-potential region (4.8 V) cannot be completely ignored, this behavior can be rationally explained by considering the changes in lattice volume and phase transitions in association with the possible amount of inserted excess Li^+ ions. Codoping, particularly in the case of highly fluorinated $LNMCOF_x$, was concluded to increase cyclability, as no obvious capacity retention enhancement was observed for the *Fd*-3*m*-type $LNMO_{4-d}$/Li cell. As extra Li^+ ions were homogeneously inserted into empty octahedral 16c sites, we believe that codoping provided a space with a suitable coordination environment for the insertion of Li^+ ions into empty octahedral sites within the spinel framework. The Jahn-Teller distortion of Cu^{2+} ions along the *a*-axis and that of Mn^{3+} ions along the *b*-axis may also contribute to the volume expansion of the 16c octahedral empty sites, which may help to suppress the cubic-to-tetragonal phase transition.

Finally, we compare of both the maximum specific capacity and the cyclability with previously reported Li-rich LNMOs.[45-49] The relationship between the ordering of the Ni/Mn arrangement and the maximum specific capacity under potential window from 4.9-2.0 V tended to be the same with previous data,[45-49] the dually incorporated $LNMCOF_{0.06}$ showed larger specific capacity of ca. 284 mAh·g^{-1} than ordered LNMO of <270 mAh·g^{-1} and disordered LNMO of <250 mAh·g^{-1}, respectively. In contrast, disordered LNMO maintained a high-capacity retention after cycles, at the expense of the maximum specific capacity, compared to the ordered phase. Interestingly to note that the effect of dual substitution was also clearly observed in cycle characteristics. The capacity retention does not linearly degreased respect to the number of cycles in the cyclability tests of many reported half-cells, but often observed nonlinear decrease at certain cycles. This is due to a micro-internal short circuit formation in the battery caused by the leaching of transition metal cations, especially manganese ions, from the positive electrode into the electrolyte. Since the capacitance decay observed in the $LNMCOF_{0.12}$ electrode was linear, the effect of the F substitution on the suppression of the electrolytic decomposition reaction observed in the high-potential state would be significantly.

Conclusions

The effects of F^-/Cu^{2+} codoping on the formation of intrinsic F_{vo} and Cu_{Mn} defects in the LNMO spinel framework and the influence of this codoping on the Li^+ storage and transport properties of LNMO were studied using theoretical and experimental techniques. The modification of the cation and anion coordination environment upon codoping was found to change the crystal morphology, increase the volume of empty octahedral 16c sites, reduce the activation energy of Li^+ hopping along the 8c–4a/12d–8c route, and mitigate the cubic-to-tetragonal phase transition to achieve high specific capacity, C-rate capability, and cyclability. In light of these findings, we believe that material design approaches based on doping with multiple elements, including both metal cations and anions, provide a new direction for the fabrication of high-energy and high-power-density active materials for advanced LIBs.

Experimental Section

Growth and characterization of LNMCOFs. LNMO crystals were grown from a eutectic mixture of LiCl–KCl flux,[25,28] and co-substitution of F^- and Cu^{2+} into the LNMO lattice via the formation of a substitutional solid solution ($LiNi_{0.49}Mn_{1.49}Cu_{0.01}O_4$, LNMCO) was achieved by two-step flux growth. In the first step, a trace amount of Cu^{2+} was incorporated using a stoichiometric amount of $Cu(NO_3)_2{\cdot}3H_2O$, and the subsequent introduction of F− was realized by reacting LNMCO with LiF–KCl flux at 800 °C for 20 h. The prepared powder was washed in warm water to remove residual flux and annealed at 700 °C for 10 h in an atmosphere of O_2. Crystal structures were examined by X-ray diffraction (XRD; Rigaku, SmartLab; 40 kV, 30 mA) using a scan range of 2θ = 10–80° and Cu Kα radiation. Microstructures were observed by field-emission scanning electron microscopy at 10 kV (FE-SEM; JSM-7600F, JEOL), while chemical compositions were examined by inductively coupled plasma optical emission spectroscopy (ICP-OES, SPS5510) and X-ray photoelectron spectroscopy (XPS; JPS-9010MX, JEOL; 15 kV, 15 mA, monochromic Al Kα source). The arrangements of Ni and Mn in crystals were characterized by Raman spectroscopy (532-nm excitation; LabRAM, Horiba, Japan). Electrodes were prepared by a conventional pasting technique. Specifically, a paste containing the active material, acetylene black, and polyvinylidene fluoride (90:5:5, w/w) was diluted with N-methyl-2-pyrrolidone to a viscosity of 5.1 Pa s and coated on 20-μm-thick Al foil using an applicator. The loading amount (10 mg/cm^2) and tap density (~3.0 g/cm^3) were set to values close to those of commercial LIB cells, and the coated electrode was dried in a vacuum oven at 120 °C for 24 h. For electrochemical characteristics investigation, a coin-type

cell (R2032) was assembled in an Ar-filled glovebox (MIWA MFG Co., Ltd., controlled H2O level of <1 ppm.) using Li metal (Honjo Metal Co., Ltd.) as a counter electrode, a porous polypropylene film (Celgard, #2500) as a separator, and a condensed paste containing 1 M LiPF6 in a mixture of ethylene carbonate (EC) and dimethyl carbonate (DMC) (3:7, v/v) as an electrolyte. Galvanostatic charge-discharge tests were conducted in cut-off voltage ranges of 3.5–4.8 and 2.0–4.8 V (vs. Li^+/Li) using a battery tester (HJ1001SD8, HOKUTO DENKO). Electrochemical impedance spectroscopy (EIS) measurements were performed in a frequency range of 2 MHz to 1 mHz using a VSP-300 electrochemical workstation (Bio-logic). All electrochemical measurements were performed in a constant-temperature chamber (Espec, SU-221) at 25 °C.

DFT calculations. DFT calculations were performed using the generalized gradient approximation (GGA-PBEsol) + U and projector-augmented wave methods as implemented in the Vienna *ab initio* simulation package (VASP).[34–36] The U values for the *d*-orbitals of Ni, Mn, and Cu were set to 6.0, 3.9, and 4.0 eV, respectively.[37–39] According to previous reports, the magnetic ground state of LNMO exhibits ferrimagnetic ordering (Ni↓Mn↑),[40–42] and ferrimagnetic spin configurations were therefore used for all calculations. An energy cut-off of 500 eV and a 3 × 3 × 3 *k*-point mesh was used for the superstructure of 56 atoms in a cubic spinel lattice of 8($LiNi_{0.5}Mn_{1.5}O_4$) with $P4_332$ symmetry as a starting structure. To realize the atomic arrangement of 8($LiNi_{0.5}Mn_{1.375}Cu_{0.125}O_{4-x}F_x$) ($0.125 \le x \le 0.375$), one to three F^- anions were incorporated into the possible 24*e* and 8*c* O oxygen sites in the unit cell of $LiNi_{0.5}Mn_{1.375}Cu_{0.125}O_{4-x}F_x$ ($0.125 \le x \le 0.375$). The nudged elastic band method was used to investigate the minimum energy pathways of Li^+ hopping from a given lattice position to adjacent sites.[43] Crystal structure relaxation was allowed for all calculations, and the final energies of optimized geometries were recalculated to correct for changes of the plane-wave basis during relaxation.

Author Contributions

D. K and N. Z. contributed the synthesis, preparation and electrochemical characterization of the LNMCOFx electrodes, H. S and N. Z. contributed the computational study of the LNMCOFx crystals. D. K., H.S and N. Z. contributed drafting of this paper. N. Z. and K. T. contributed to make the concept and design of this study.

Conflicts of interest

There are no conflicts to declare.

Acknowledgements

This work was supported by JST-CREST (JPMJCR21B, JPMJCR1322) JAPAN. N.Z. further acknowledge JSPS KAKENHI (19H04693, 17H01322). The crystal structures were drawn with VESTA[44].

Notes and references

1 M. M. Thackeray, C. Wolverton, E. D. Isaacs, Electrical Energy Storage for Transportation—Approaching the Limits of, and Going Beyond, Lithium-Ion Batteries. Energy Environ. Sci. 5, 7854–7863 (2012).
2 D. A. Notter, M. Gauch, R. Widmer, P. Wäger, A. Stamp, R. Zah, H.-J. Althaus, Contribution of Li-Ion Batteries to the Environmental Impact of Electric Vehicles. Environ. Sci. Technol. 44, 7744–7744 (2010).
3 S. K. Martha, et al. On the Thermal Stability of Olivine Cathode Materials for Lithium-Ion Batteries. J. Electrochem. Soc. 158, A1115 (2011).
4 F. Lin et al. Surface reconstruction and chemical evolution of stoichiometric layered cathode materials for lithium-ion batteries. Nature Commun. 5, 3529 (2014).
5 M.-J. Lee, S. Lee, P. Oh, Y. Kim, J. Cho, High Performance LiMn2O4Cathode Materials Grown with Epitaxial Layered Nanostructure for Li-Ion Batteries. Nano Lett. 14, 993–999 (2014).
6 A. Yamada, S. C. Chung, K. Hinokuma, Optimized LiFePO4 for Lithium Battery Cathodes. J. Electrochem. Soc. 148, A224–A229 (2001).
7 J. Lee, et al. A new class of high capacity cation-disordered oxides for rechargeable lithium batteries: Li–Ni–Ti–Mo oxides. Energy Environ. Sci. 8, 3255–3265 (2015).
8 N. Nitta, F. Wu, J. T. Lee, G. Yushin, Li-ion battery materials: present and future. Materials Today 18, 252–264 (2015).
9 V. Etacheri, R. Marom, R. Elazari, G. Salitra, D. Aurbach, Challenges in the development of advanced Li-ion batteries: a review. Energy Environ. Sci. 4, 3243–21 (2011).
10 A. Manthiram, K. Chemelewski, E. S. Lee, A perspec-tive on the high-voltage LiNi0.5Mn1.5O4 spinel cathode for lithium-ion batteries. Energy Environ. Sci. 7, 1339–1350 (2014).
11 G. Q. Liu, L. Wen, Y. M. Liu, Spinel LiNi0.5Mn1.5O4 and its derivatives as cathodes for high-voltage Li-ion batteries. J Solid State Electrochem 14, 2191–2202 (2010).
12 S. Tan, Y. J. Ji, Z. R. Zhang, Y. Yang, Recent Progress in Research on High-Voltage Electrolytes for Lithium-Ion Batteries. ChemPhysChem 15, 1956–1969 (2014).
13 H. Wang et al. A New Strategy to Stabilize Capacity and Insight into the Interface Behavior in Electrochemical Reaction of LiNi0.5Mn1.5O4/Graphite System for High-Voltage Lithium-Ion Batteries. ACS Appl. Mater. Interfaces 9, 33274–33287 (2017).
14 A. M. Haregewoin, A. S. Wotango, B. J. Hwang, Electrolyte addi-tives for lithium ion battery electrodes: progress and perspectives. Energy Environ. Sci. 9, 1955–1988 (2016).
15 N.-S. Choi, J.-G. Han, S.-Y. Ha, I. Park, C.-K. Back, Recent advances in the electrolytes for interfacial stability of high-voltage cathodes in lithium-ion batteries. RSC Adv. 5, 2732–2748 (2015).
16 M. Gauthier et al. Electrode–Electrolyte Interface in Li-Ion Batteries: Current Understanding and New Insights. J. Phys. Chem. Lett. 6, 4653–4672 (2015).
17 E. S. Lee, K. W. Nam, E. Hu, A. Manthiram, Influence of Cation Ordering and Lattice Distortion on the Charge–Discharge Behavior of LiMn LiNi0.5Mn1.5O4 Spinel between 5.0 and 2.0 V. Chem. Mater. 24, 3610–3620 (2012).
18 K. Shimoda, et al. Delithiation/Lithiation Behavior of LiNi0.5Mn1.5O4 Studied by In Situ and Ex Situ 6,7Li NMR Spectros-copy. J. Phys. Chem. C 119, 13472–13480 (2015).
19 J. Yoon, M. Jeong, I. T. Bae, K. W. Nam, W.-S. Yoon, Zr-doping effect on the capacity retention of LiNi0.5Mn1.5O4–δ cycled between 5.0 and 1.0 V: In situ synchrotron X-Ray diffraction study. J. Power Sources 368, 1–10 (2017).

20 R. Alcántara et al. Changes in the Local Structure of LiMgyNi0.5-yMn1.5O4 Electrode Materials during Lithium Extraction. Chem. Mater. 16, 1573–1579 (2004).
21 J. Liu, A. Manthiram, Understanding the Improvement in the Electrochemical Properties of Surface Modified 5 V LiMn1.42Ni0.42Co0.16O4 Spinel Cathodes in Lithium-ion Cells. Chem. Mater. 21, 1695–1707 (2009).
22 K. R. Chemelewski, A. Manthiram, Origin of Site Dis-order and Oxygen Nonstoichiometry in LiMn1.5Ni0.5– xMxO4 (M = Cu and Zn) Cathodes with Divalent Dopant Ions. J. Phys. Chem. C 117, 12465–12471 (2013).
23 M. C. Yang, et al. Electronic, Structural, and Electrochem-ical Properties of LiNixCuyMn2– x– yO4 (0 < x< 0.5, 0 < y< 0.5) High-Voltage Spinel Materials. Chem. Mater. 23, 2832–2841 (2011).
24 J. Liu, A. Manthiram, Understanding the Improved Electrochemical Performances of Fe-Substituted 5 V Spinel Cathode LiNi0.5Mn1.5O4. J. Phys. Chem. C 113, 15073–15079 (2009).
25 H. Shiiba, N. Zettsu, S. Kida, K. Teshima, Impact of trace extrinsic defect formation on the local symmetry transition in spinel LiNi0.5Mn1.5O4-δ and their electrochemical characteristics. J. Mater. Chem. A, 6, 22749-22757 (2018).
26 D.-W. Kim, et al. Full picture discovery for mixed-fluorine anion effects on high-voltage spinel lithium nickel manganese oxide cath-odes. NPG Asia Mater. 9, e398 (2017).
27 D-W Kim, et al., Metastable oxysulfide surface formation on LiNi0.5Mn1.5O4 single crystal particles by carbothermal reaction with sulfur-doped heterocarbon nanoparticles: new insight into their structural and electrochemical characteristics, and their potential applications, J. Mater. Chem. A, 8 22302-22314 (2020).
28 N. Zettsu, S. Kida, S. Uchida, K. Teshima, Sub-2 Nm Thick Fluoroalkylsilane Self-Assembled Monolayer-Coated High Voltage Spinel Crystals as Promising Cathode Materials for Lithium Ion Batteries. Sci. Rep. 6, 31999 (2016).
29 J. Yang, X. Han, X. Zhang, F. Cheng, J. Chen, Spinel LiNi0.5Mn1.5O4 cathode for rechargeable lithiumion batteries: Nano vs micro, ordered phase (P4332) vs disordered phase. Nano Res. 6, 679–687 (2013).
30 J. Song et al. Role of Oxygen Vacancies on the Perfor-mance of Li[Ni0.5–xMn1.5+ x]O4 (x= 0, 0.05, and 0.08) Spinel Cath-odes for Lithium-Ion Batteries. Chem. Mater. 24, 3101–3109 (2012).
31 P. V. Sushko, K. M. Rosso, J. G. Zhang, J. Liu, M. L. Sushko, Oxygen Vacancies and Ordering of d-levels Control Voltage Sup-pression in Oxide Cathodes: the Case of Spinel LiNi0.5Mn1.5O4-δ. Adv. Funct. Mater. 23, 5530–5535 (2013).
32 E. Lee, K. A. Persson, Revealing the coupled cation interactions behind the electrochemical profile of Lix Ni0.5Mn1.5O4. Energy Environ. Sci. 5, 6047–6051 (2012).
33 C. J. Jafta, M. K. Mathe, N. Manyala, W. D. Roos, K. I. Ozoemena, Microwave-Assisted Synthesis of High-Voltage Nanostructured LiNi0.5Mn1.5O4 Spinel: Tuning the Mn 3+ Content and Electrochemical Performance. ACS Appl. Mater. Interfaces 5, 7592–7598 (2013).
34 G. Kresse, J. Furthmüller, Efficiency of ab-initio total energy calculations for metals and semiconductors using a plane-wave basis set. Comput. Mater. Sci. 6, 15–50 (1996).
35 G. Kresse, J. Furthmüller, Efficient iterative schemes for ab initiototal-energy calculations using a plane-wave basis set. Phys. Rev. B 54, 11169–11186 (1996).
36 J. P. Perdew, et al. Restoring the Density-Gradient Expan-sion for Exchange in Solids and Surfaces. Phys. Rev. Lett. 100, 136406 (2008).
37 P. E. Blöchl, Projector augmented-wave method. Phys. Rev. B 50, 17953–27 (1994).
38 A. Jain, et al. Formation enthalpies by mixing GGA and GGA +Ucalculations. Phys. Rev. B 84, 66–11 (2011).
39 T. Mueller, G. Hautier, A. Jain, G. Ceder, Evaluation of Tavorite-Structured Cathode Materials for Lithium-Ion Batteries Using High-Throughput Computing. Chem. Mater. 23, 3854–3862 (2011).
40 G. Hautier, S. P. Ong, A. Jain, C. J. Moore, G. Ceder, Accuracy of density functional theory in predicting formation ener-gies of ternary oxides from binary oxides and its implication on phase stability. Phys. Rev. B 85, 973–19 (2012).
41 N. Biškup, J. L. Martínez, M. E. Arroyo y de Dompablo, P. Díaz-Carrasco, J. Morales, Relation between the magnetic prop-erties and the crystal and electronic structures of manganese spinels LiNi0.5Mn1.5O4 and LiCu0.5Mn1.5O4−δ (0<δ<0.125). J. Appl. Phys. 100, 093908 (2006).
42 N. Amdouni, K. Zaghib, F. Gendron, A. Mauger, C. M. Julien, Magnetic properties of LiNi0.5Mn1.5O4 spinels prepared by wet chemical methods. J. Magn. Magn. Mater. 309, 100–105 (2007).
43 Y. Chen, Y. Sun, X. Huang, Origin of the Ni/Mn order-ing in high-voltage spinel LiNi0.5Mn1.5O4: The role of oxygen vacan-cies and cation doping. Comput. Mater. Sci. 115, 109–116 (2016).
44 K. Momma, F. Izumi, VESTA 3 for three-dimensional visualization of crystal, volumetric and morphology data. J. Appl. Crystallogr. 44, 1272-127 (2011).
45 M. Mancini, P. Axmann, G. Garielli, M. Kinyanjui, U. Kaiser, M. Wohlfahrt-Mehrens, ChemSusChem. 9, 1843-1849 (2016).
46 S.-H. Park, S.-W. Oh, S. H. Kang, I. Belharouak, K. Amine, Y.-K. Sun, Electrochim. Acta 52, 7226–7230 (2007).
47 S.-H. Park, S.-W. Oh, C.-S. Yoon, S.-T. Myung, Y.-K. Sun, Electrochem. Solid-State Lett. 8, A163–A167 (2005).
48 E.-S. Lee, K.-W. Nam, E. Hu, A. Manthiram, Chem. Mater. 24, 6310–6320 (2012).
49 W. Li, B. Songa, A. Manthiram, Chem. Soc. Rev., 46, 3006-3059 (2017).

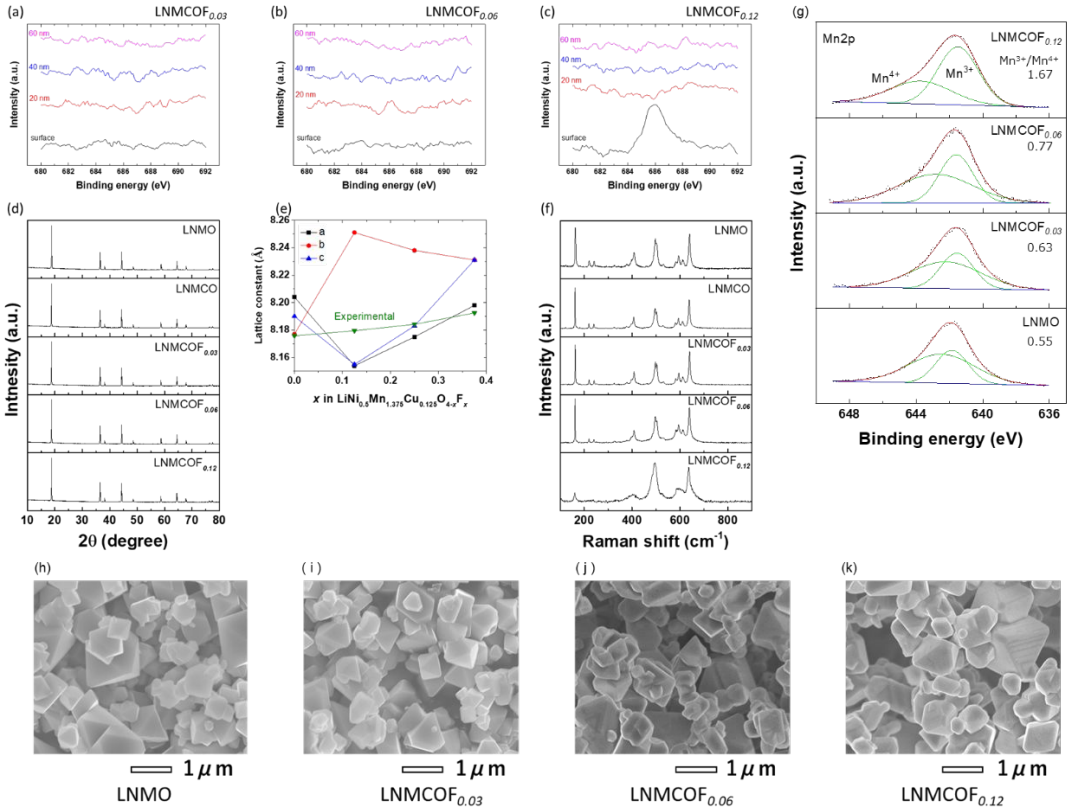

Figure 1. Structural characteristics of $LiNi_{0.5}Mn_{1.5}O_4$ and $LiNi_{0.5}Mn_{1.49}Cu_{0.01}O_{4-x}F_x$ crystals: (a–c) the F 1*s* spectra of $LNMCOF_x$ recorded for different depths from the surface, (d) powder X-ray diffraction (XRD) analysis (e) the lattice parameter (extracted from the corresponding XRD patterns) (f) Raman spectra (g) X-ray photoelectron spectroscopy (XPS) Mn 2p spectra of LNMCOF crystals. The broad peak can be deconvoluted into two peaks, which were assigned to Mn^{3+} and Mn^{4+} species (h-k) FE-SEM images.

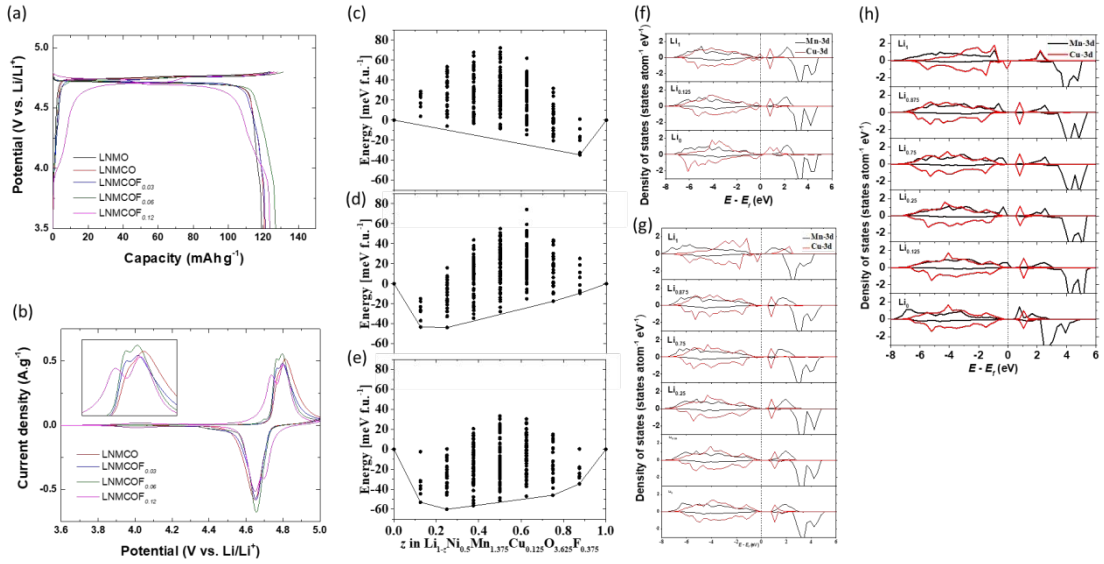

Figure 2. Electrochemical and electronic characteristics of $LiNi_{0.5}Mn_{1.5}O_4$ and $LiNi_{0.5}Mn_{1.49}Cu_{0.01}O_{4-x}F_x$ crystals: (a) Galvanostatic charge-discharge curves of the half-cells recorded at a cutoff voltage range of 3.5-4.8 V (vs. Li/Li^+) and a rate of 0.2 C. (b) Cyclic voltammograms conducted with a 0.15 mV/s scan rate from 3.5 to 5 V. (c-e) Formation energy as a function of Li composition in DFT-modeled $LiNi_{0.5}Mn_{1.375}Cu_{0.125}O_{4-x}F_x$ frameworks (x = 0.125, 0.25, 0.375): (c) x = 0.125, (d) x = 0.25, and (e) x = 0.375. (f-h) DFT-calculated partial density of states (PDOS) for the Mn 3*d* and Cu 3*d* orbitals in $LiNi_{0.5}Mn_{1.375}Cu_{0.125}O_{4-x}F_x$ materials with various Li contents: (f) x = 0.125, (g) x = 0.25, and (f) x = 0.375.

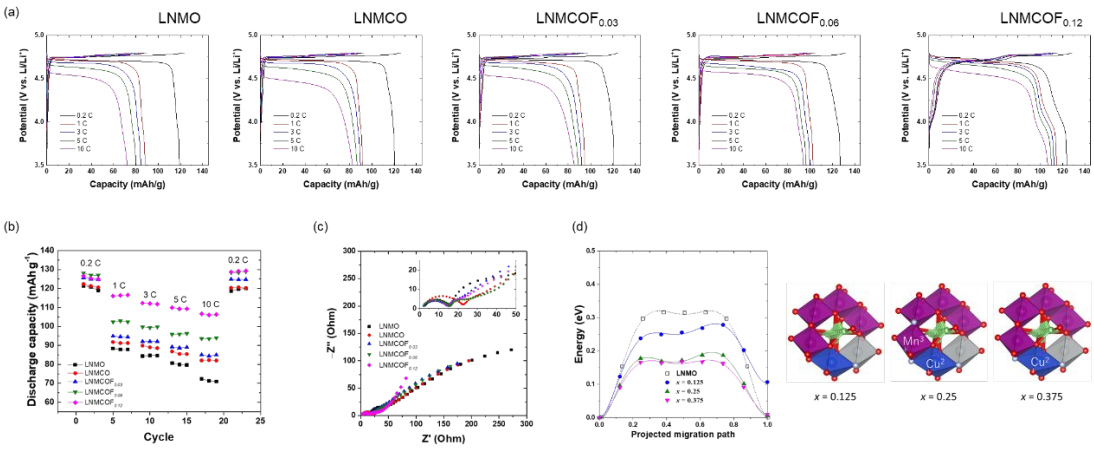

Figure 3. Lithium-ion transportation characteristics in $LiNi_{0.5}Mn_{1.5}O_4$ and $LiNi_{0.5}Mn_{1.49}Cu_{0.01}O_{4-x}F_x$ crystals: (a) Galvanostatic charge-discharge profiles of LNMO, LNMCO, and series of LNMCOF*x* electrodes based half-cells with various C-rate under controlled in cut-off voltage range of 4.8-3.5 V (Li^+/Li) (b) C-rate capabilities of the half-cells were determined by systematic galvanostatic charge-discharge testing at various current densities with cut-off voltage range of 4.8-3.5 V (Li^+/Li) (c) Nyquist plot of the examined half-cells. The kinetic parameters were determined by EIS approaches. The Nyquist plots were fitted using the equivalent circuit model. The high and low frequency semicircles are attributed to surface film resistance (R_{sf}: CEI layer) and charge transfer resistance (R_{ct}) at the electrode/electrolyte interface, respectively. The Li-ion diffusion coefficient from the relation between the real impedance and the angular frequency in the low frequency region were further estimated to quantitatively evaluate the F- substitution effects. (d) The trajectory of Li^+ migration along the most energetically preparable 8c–4a/12d–8c pathway in the spinel framework and the activation energy for the corresponding Li^+ hopping was studied using DFT calculations.

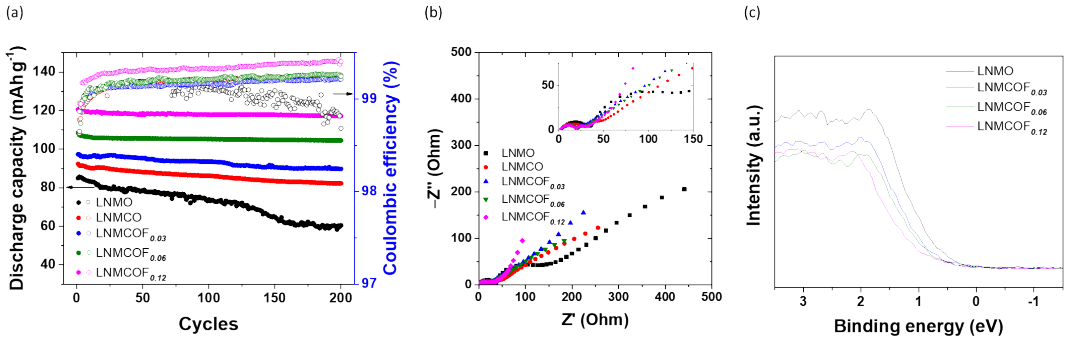

Figure 4. The effect of Cu^{2+} and F^- doping on cyclability performed at a cutoff voltage of 3.5–4.8 V a 0.2 C rate. (a) Discharge capacity vs. cycle number of the half-cells which were determined by galvanostatic charge-discharge testing at 23 °C (b) Nyquist plot of the 200 cycled half-cells. (c) XPS valence band spectra of the $LiNi_{0.5}Mn_{1.5}O_4$ and $LiNi_{0.5}Mn_{1.49}Cu_{0.01}O_{4-x}F_x$ crystals.

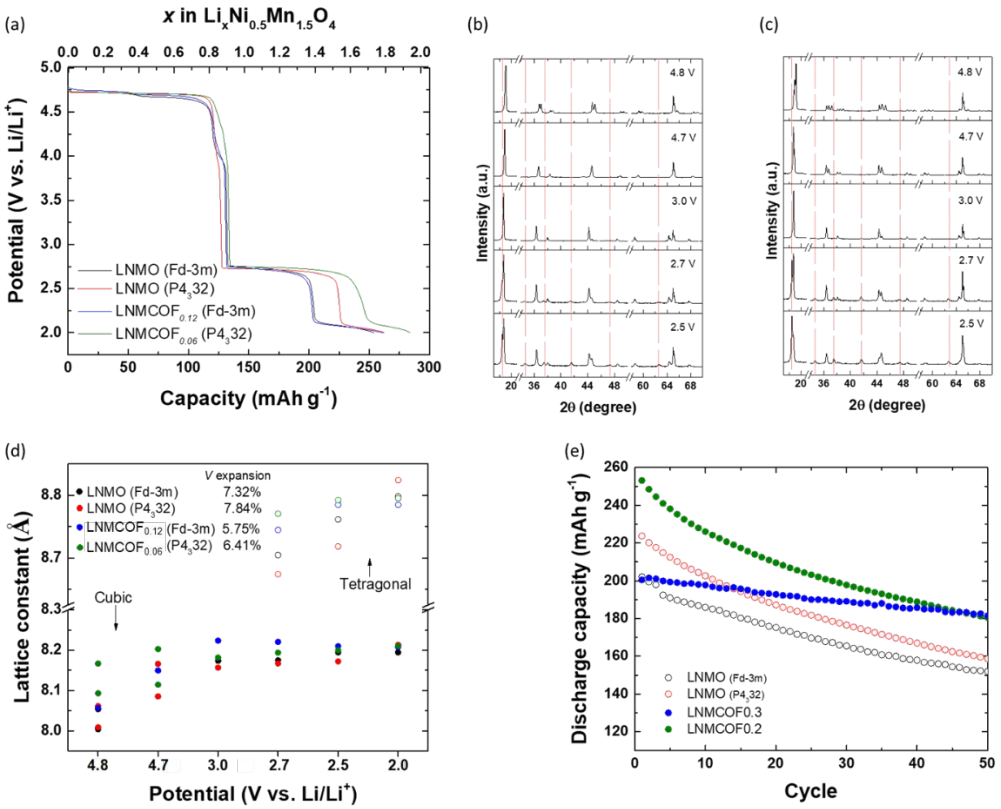

Figure 5. The synergistic effects of Cu^{2+}/F^- codoping on the reversible specific capacity of Li-rich spinel-type $Li_{1+y}Ni_{0.5}Mn_{1.5}O_4$. (a) discharge profiles based on the extra lithiation reaction by galvanostatic discharge tests at a cutoff voltage extended to 2.1 V. (b, c) *ex situ* XRD profiles of $LNMCOF_{0.12}$ (b) and $LNMCOF_{0.06}$ (c) electrodes with various states of charge, with the peaks of the tetragonal phase. (d) Effects of applied potential (4.8–2.0 V) on the lattice constant and lattice volume of LNMO, $LNMCOF_{0.06}$, and $LNMCOF_{0.12}$ crystals determined from ex situ XRD profiles. (e) Discharge capacity vs. cycle number of the half-cells which were determined by galvanostatic charge-discharge testing at a cutoff voltage of 4.8–2.0 V.